INSTRUMENTATION FOR TEMPERATURE AND HEAT FLUX MEASUREMENT ON A SOLID SURFACE UNDER BWR OPERATING CONDITIONS

M. Bergagio, S. Hedberg, S. Rydström and H. Anglart
Department of Physics, KTH Royal Institute of Technology, AlbaNova University Center,
106 91 Stockholm, Sweden
bergagio@kth.se

ABSTRACT

A new experimental facility has been developed at KTH Royal Institute of Technology to measure temperature and heat flux propagations in solid walls due to mixing of non-isothermal water streams in their vicinity. The main purpose of the measurements has been to obtain a high-precision experimental database suitable for validation of Computational Fluid Dynamics (CFD) codes. Consequently, a set of experiments have been performed in a test section simulating the annular region in the BWR control-rod guide tubes. Since preliminary CFD results implied that 0.1-1 Hz temperature oscillations were to be expected, this experimental research intends to assess the magnitude of temperature fluctuations within the abovementioned frequency range. To this end, water and wall temperatures have been measured in the innermost part of the test-section annulus, with a variety of boundary conditions. As thermocouples would otherwise be available at few axial and azimuthal coordinates only, the tube they are installed on has been lifted, lowered and rotated by a software-controlled motor to record temperature fluctuations in the whole mixing region. At each measurement point, data have been collected over a time long enough to detect the existence of the aforesaid fluctuations. Moreover, an uncertainty analysis has been carried out concerning water temperatures. Thermocouples meant to monitor these temperatures have been modelled with a finite-element method for this very purpose. The wall heat flux has also been estimated using experimental data, thanks to a corrected finite-difference Crank-Nicolson scheme.

1. INTRODUCTION

The reader should refer to the introduction in [1] for a broader introduction to the problem of thermal fatigue in BWRs; hence, here we will just recall that this study investigates thermal fatigue, believed to have caused the break of a control rod stem at Oskarshamn 3 and of another one at Forsmark 3, together with cracks in the stem of many control rods in both reactors [1]. Thus, comparably to the actual plant layout, in our experiments two turbulent water streams at either 60 °C or 150 °C mix with other two at 276 °C, in the vertical annulus between an inner and an outer tube. Water and wall temperatures are recorded at the wet surface of the inner tube and at various depths in it respectively, since the inner tube replicates the BWR control-rod stem affected by thermal fatigue-induced stresses.

This article focuses on estimating uncertainty levels in the water temperature time series exemplified in [1], and on evaluating the radial heat flux at the wet surface of the inner tube.
The uncertainty associated with our measurements is explored here since this topic has not been covered in [1]. Instead of examining end-to-end calibration data [2], uncertainty is determined by dividing the data acquisition system (DAS) into three components, whose contribution to the total uncertainty is

taken to be independent of one another. A fourth uncertainty source, sprouting from the thermocouple placement and geometry, is also accounted for.

As regards the radial heat flux, several approaches can be found in literature for deriving it from experimental data (see, e.g., [3] and [4]). We have been specifically requested to find the radial heat flux in the vicinity of water-side thermocouples; therefore, a fast method to approximate this variable is proposed here, based on a finite-difference Crank-Nicolson scheme that resorts to the few water temperature series available at each axial level z.

2. MOUNTING OF THERMOCOUPLES IN THERMOCOUPLE DISCS

Before addressing the topics outlined in the introduction, it is worth to illustrate how thermocouples have been installed in the wall of the inner tube, since we will return to this point later.
First, however, we must stress that our original goal was to solve the inverse heat conduction problem (IHCP) thanks to smoothed wall-temperature readings. Thus, 6 ~0.7 mm Ø blind holes were drilled for housing the necessary 0.5 mm Ø K-type thermocouples. These holes were drilled with a mill machine in the mid thermocouple disc [1] from its back surface to different depths. This disc, as well as the left and right ones, has a diameter of 11.90 mm and an upper surface whose curvature matches the one of the inner tube [1].
A number of papers can be found in literature where the thermocouple is welded to the bottom of its hole (i.e., embedded [5]) for similar purposes. However, since welded thermocouples usually require special equipment and big holes that could sensibly modify the temperature distribution in the thermocouple disc, here casings were used for housing the thermocouples, similarly to [6]. These casings, hollow cylinders measuring 0.7 mm at their outer diameter and varying in length to make soldering easier, were partially inserted into the holes and then silver-soldered to the back surface of the thermocouple disc. After that, each thermocouple was pushed through its casing into the corresponding hole until its tip made contact with the bottom of the hole. The thermocouple was then kept in position by soldering it to the casing with a high-temperature solder ($\sim 600 - 700$ °C).
Other casings were soldered to the 6 ~0.7 mm Ø through holes that house the 0.5 mm Ø K-type thermocouples measuring water temperature (see Fig. 1), henceforth called H1, H2, H3, H4, V1 and V4. These holes were drilled in the left and right thermocouples discs [1]. In this case, each thermocouple was inserted into a hole until its tip lay at $r_0 = 17.5$ mm, which identifies the water-exposed surface of the inner tube [1].
Finally, all thermocouple discs were TIG welded to the inner tube at the interface with its wet surface.
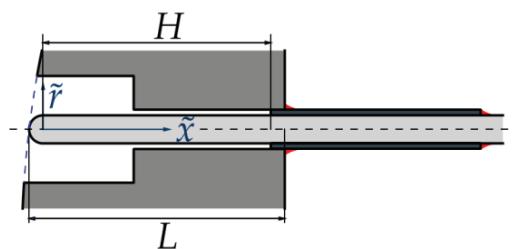
Fig. 1. Longitudinal section of the thermocouple after insertion in the thermocouple disc. Light gray: thermocouple; gray: thermocouple disc; dark gray: casing; red: high-temperature solder.

3. UNCERTAINTY

3.1. Methodology

Before proceeding any further, it should be clarified that the analysis outlined here concerns the 0.5 mm Ø K-type thermocouples for water temperature only, as they are of primary importance in our study.

In our experimental setup, the thermocouple signals are acquired by the NI SCXI-1102 module in an NI SCXI-1000 chassis, and then transferred through the A/D converter of an NI DAQ-6024E card to a laptop for data recording and processing. This being said, four uncertainty sources, here shown as tuples, are taken into account:

- the intrinsic accuracy (B_{TC}^+, B_{TC}^-) of the K-type, ungrounded thermocouple;
- the absolute accuracy (B_{DAQ}^+, B_{DAQ}^-) of the DAQ-6024E card;
- the absolute accuracy (B_{SCXI}^+, B_{SCXI}^-) of the SCXI-1102 module;
- the thermocouple mounting error $(B_{mount}^+, B_{mount}^-)$.

All uncertainty sources are assumed to be independent of one another. This hypothesis simplifies the following analysis considerably – see Eq. (16).

As concerns the intrinsic accuracy of the thermocouples under study, it is equal to $B_{TC}^+ = |B_{TC}^-| = 1.5\,°C$ [7], since these thermocouples are supplied with IEC 60584-2 Class 1 accuracy as standard [8] and the highest water temperature is lower than 375 °C.

With regard to the DAQ-6024E card, its accuracy is evaluated according to the guidelines in [9], with the voltage-temperature relationship from [10], and offset, noise and percent-of-reading components of the absolute accuracy from [11]. Biases B_{DAQ}^+ and B_{DAQ}^- are listed in Table I.

Concerning the accuracy of the SCXI-1102 module, the same procedure holds as for the DAQ-6024E card, this time with values from [9]. Biases B_{SCXI}^+ and B_{SCXI}^- are also shown in Table I.

As to the thermocouple mounting error, it is estimated by solving a simplified heat equation [12]

$$\rho \hat{C}_p \frac{\partial T}{\partial t} = \nabla \cdot (k\,\nabla T) \tag{1}$$

on the thermocouple domain. Eq. (1), expressed in cylindrical coordinates, is written in the weak form and implemented in the finite element software FreeFem++ [13] with a Crank-Nicolson scheme.
In order to reduce the dimensionality of the problem at hand to two, a lead-wire model (also known as single-wire or one-wire model) is introduced, which combines Chromel and Alumel wires into an equivalent one, characterized by a radius $r_1 = \sqrt{2}\,r_{Chromel}$, $r_{Chromel} = r_{Alumel}$ (see [14, 15, 16, 17]). Postulating a perfect contact between the insulator and the outer protective sheath [18] and modeling the sheath as a hollow cylinder and the thermocouple tip as a hemisphere also help to develop a simplified two-dimensional model.
As the problem is now axisymmetric, differential normal area, gradient and differential volume can be written in cylindrical coordinates discarding any contribution from azimuthal components, so that the weak formulation of Eq. (1) is obtained as

$$\iint_S \rho \hat{C}_p \frac{\partial T}{\partial t} w\,\tilde{r}\,d\tilde{r}\,d\tilde{x} = -\iint_S k \left(\frac{\partial T}{\partial \tilde{r}} \frac{\partial w}{\partial \tilde{r}} + \frac{\partial T}{\partial \tilde{x}} \frac{\partial w}{\partial \tilde{x}} \right) \tilde{r}\,d\tilde{r}\,d\tilde{x}$$
$$+ \int_{\Gamma_{\tilde{r}}} k \frac{\partial T}{\partial \tilde{r}} w\,\tilde{r}\,d\tilde{x} + \int_{\Gamma_{\tilde{x}}} k \frac{\partial T}{\partial \tilde{x}} w\,\tilde{r}\,d\tilde{r} . \tag{2}$$

Robin boundary conditions are supplied at every edge of the domain, which implies that

$$\int_{\Gamma_\xi} k \frac{\partial T}{\partial \xi} w\,\tilde{r}\,d\psi = -\int_{\Gamma_\xi} h \left(T - T_f \right) w\,\tilde{r}\,d\psi , \qquad (\xi, \psi) = (\tilde{r}, \tilde{x}) \text{ or } (\tilde{x}, \tilde{r}) , \tag{3}$$

where the heat transfer coefficient obeys Eqs. (4) and (5)

$$h: \begin{cases} h|_{\tilde{r}=r_3, \ \tilde{x}\geq 0} \equiv h|_{\tilde{x}^2+\tilde{r}^2=r_3^2, \ \tilde{x}\leq 0} = 17000 \ \mathrm{W}/\mathrm{m^2K} & (4) \\ h|_{\tilde{r}=0} \equiv h|_{\tilde{x}=H} = 0 \text{ from symmetry and adiabatic boundary conditions respectively,} & (5) \end{cases}$$

while the fluid temperature changes with time according to Eq. (6)

$$T_f = T_0 + \Delta T \sin(2\pi f t), \tag{6}$$

with $f = 2$ Hz, $T_0 = 397.95$ K and $\Delta T = 10$ K. As to length H and radius r_3, they are shown in Fig. 1 and Fig. 2 respectively; specifically, r_3 refers to the outer radius of the thermocouple sheath, r_2 being the inner one.

Now, applying the Crank-Nicolson scheme, Eq. (2) is rearranged as

$$
\begin{aligned}
\iint_S \rho \hat{C}_p \frac{T_h^{p+1} - T_h^p}{\Delta t} w_h \, \tilde{r} \, d\tilde{r} \, d\tilde{x} = &-\frac{1}{2} \int_{\Gamma_{\tilde{r}}} h \left(T_h^{p+1} + T_h^p - T_f^{p+1} - T_f^p \right) w_h \, \tilde{r} \, d\tilde{x} \\
&- \frac{1}{2} \int_{\Gamma_{\tilde{x}}} h \left(T_h^{p+1} + T_h^p - T_f^{p+1} - T_f^p \right) w_h \, \tilde{r} \, d\tilde{r} \\
&- \frac{1}{2} \iint_S k \left[\frac{\partial w_h}{\partial \tilde{r}} \frac{\partial \left(T_h^{p+1} + T_h^p \right)}{\partial \tilde{r}} + \frac{\partial w_h}{\partial \tilde{x}} \frac{\partial \left(T_h^{p+1} + T_h^p \right)}{\partial \tilde{x}} \right] \tilde{r} \, d\tilde{r} \, d\tilde{x},
\end{aligned}
\tag{7}
$$

where properties k, ρ and $\hat{C}_p$ are evaluated at temperature T_h^p. As to the materials constituting these K-type thermocouples, the sheath was manufactured from Inconel 600, while MgO was chosen as insulator. Thermal properties for MgO, single-wire equivalent and Inconel 600 are computed from functions provided with the Material Properties Database (MPDB) software [19]. Thanks to Eqs. (4) and (6), the present model can be verified by comparison with [20], where an analytical expression is given for the radial temperature distribution in a thermocouple immersed in a fluid at temperature $T_f(t)$. In the same article it is postulated that a thermocouple can be broken down into a number of concentric cylindrical layers, each of them with a constant α and known Bi at its boundaries. In accordance with the examples in [20], three such layers are identified for the K-type thermocouple probe under study – namely, the single-wire equivalent, the MgO insulator and the Inconel sheath –, each with α evaluated at T_0. In the single-wire region α is calculated as

$$\alpha_{sw} = 2 \frac{k_{Chromel} + k_{Alumel}}{(\rho_{Chromel} + \rho_{Alumel})(\hat{C}_{p,Chromel} + \hat{C}_{p,Alumel})}, \tag{8}$$

while Bi is given by

$$Bi: \begin{cases} Bi \to \infty & \text{at } \tilde{r} = r_1 \text{ and } \tilde{r} = r_2 & (9) \\ Bi = \dfrac{h|_{\tilde{r}=r_3} r_3}{k_{Inconel}} & \text{at } \tilde{r} = r_3 & (10) \end{cases}$$

in view of the postulated perfect thermal contact of the insulator with both the sheath and the single wire. The heat-transfer coefficient $h|_{\tilde{r}=r_3}$ is defined in Eq. (4).

As to the computational domain, a view of the finite element (FE) mesh can be seen in Fig. 3.
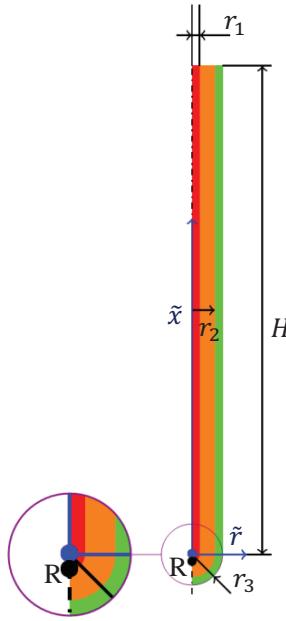
Fig. 2. Thermocouple model. Red: single-wire equivalent; orange: insulator; green: sheath.
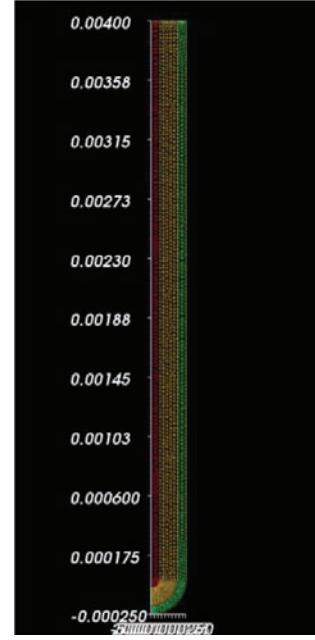
Fig. 3. FE mesh.
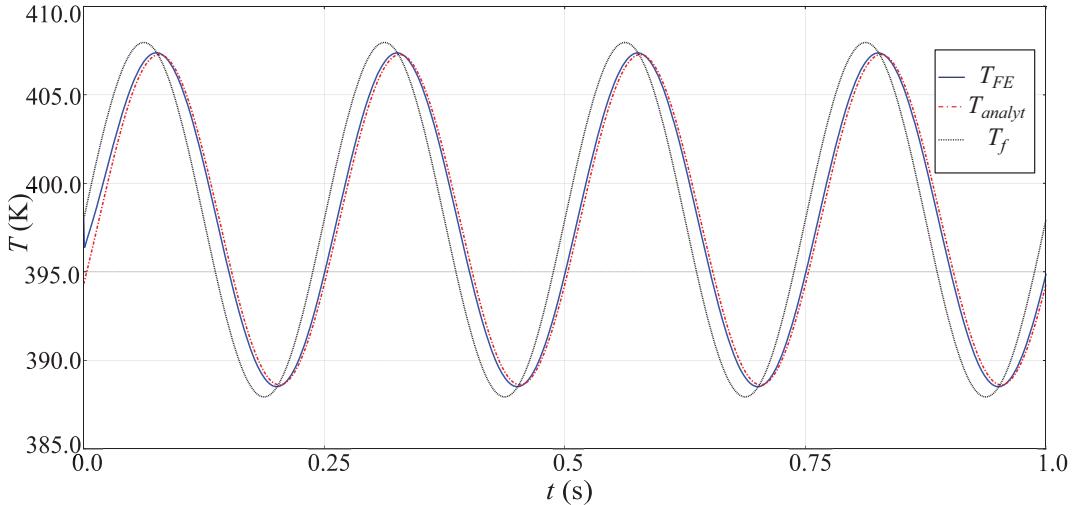
Fig. 4. Comparison of analytical and FE results at point R (referred to as T_{analyt} and T_{FE} respectively) with $f = 2\,Hz$, $T_0 = 397.95\,K$ and $\Delta T = 10\,K$. The corresponding T_f is plotted as well.

Fig. 4 establishes a comparison between FE results and the analytical solution from [20]. The agreement between the two models is quite good, at least with h as high as in Eq. (4) and with the assumption of perfect thermal contact between the insulator and the adjacent materials.

Coming now to the assessment of the thermocouple mounting error, the Robin boundary conditions in Eq. (7) is replaced with Dirichlet ones at $\Gamma_1 : (\tilde{r} = r_3,\ \tilde{x} \geq 0)$ and $\Gamma_2 : (\tilde{x}^2 + \tilde{r}^2 = r_3^2,\ \tilde{x} \leq 0)$. The temperature discussed in the further analysis, hereinafter called T_{FE}, is reached in the lowest part of the single-wire region (at point R in Fig. 2), while the temperature on boundaries Γ_1 and Γ_2 is named T_b.

In a more rigorous approach, one would determine T_b from an IHCP since, in fact, a good estimate T_{DAQ} of T_{FE} is returned by the data acquisition function, while T_b is unknown. However, given that the thermocouple mounting error is a function of $\Delta T_{FE} = T_{FE} - T_b$ (see Eqs. (13) and (14)) and our primary concern is the order of magnitude of this error, our method aims to calculate T_{FE} by substituting the known T_{DAQ} for T_b.

As can be already guessed, T_{DAQ} is assumed constant over Γ_1 and Γ_2 because the thermocouples monitoring water temperature are inserted into narrow, short horizontal holes, where water velocity is expected to decrease as the flow approaches the casing surface (see Fig. 1).

Turning to another issue, T_{DAQ} at time t, henceforth called T_b^p, is not uniquely defined because, as said in Section 2, 6 thermocouples measure water temperatures, which are then stored in 6 arrays (one per thermocouple); that is,

$$T_b^p = \widehat{\boldsymbol{T}}_f[1,j], \ \ 1 \le j \le A, \tag{11}$$

where array $\widehat{\boldsymbol{T}}_f$ in Eq. (11) could be any of the aforesaid arrays after being detrended. Detrending is necessary to derive reliable values for frequencies and variance of T_{FE}, in that both parameters are expected to play a role in the thermocouple transfer function – see, e.g., [16], where this function is related to frequency and amplitude of T_b.

Carrying out an FE analysis for each of the 6 temperature arrays would be infeasible, as they are created for any (θ_Q, z_Q) pair in the 3 entries of the experimental matrix [1]. Thus, a parameter $\hat{p}$ is introduced, accounting for the standard deviation and discrete Fourier transform (DFT) of each array

$$\hat{p} = w_1 \frac{\sigma(\widehat{\boldsymbol{T}}_f)}{\sigma_{f,max}} + (1 - w_1) \frac{I_{DFT,1}(\widehat{\boldsymbol{T}}_f)}{I_{DFT,2}(\widehat{\boldsymbol{T}}_f)}, \tag{12}$$

where $\sigma_{f,max}$ is the maximum standard deviation of all the detrended temperature measurements and $I_{DFT,1}$ is the integral of the DFT between $f = 0.1$ Hz and $f = 1$ Hz, whereas $I_{DFT,2}$ is the integral of the DFT up to $f = 4$ Hz.

Given that $(\widehat{\boldsymbol{T}}_f[1,j] - \boldsymbol{T}_{FE}[1,j])$ in Eqs. (13) and (14) is heavily dependent on $\hat{p}$, the temperature array with the highest $\hat{p}$ is selected as the ultimate $\widehat{\boldsymbol{T}}_f$ and included in a modified Eq. (7) – via Eq. (11) – with Dirichlet boundary conditions at Γ_1 and Γ_2. As a result, the ultimate $\widehat{\boldsymbol{T}}_f$ leads to the ultimate $\boldsymbol{T}_{FE}$ in Eqs. (13) and (14), which yield mean error and sample standard deviation as

$$\overline{err} = \frac{1}{A} \sum_{j=1}^{A} (\widehat{\boldsymbol{T}}_f[1,j] - \boldsymbol{T}_{FE}[1,j]) \tag{13}$$

and

$$\sigma_{err} = \sqrt{\frac{1}{A-1} \sum_{j=1}^{A} (\widehat{\boldsymbol{T}}_f[1,j] - \boldsymbol{T}_{FE}[1,j])^2} \tag{14}$$

respectively. After that, a $\sigma_{bias,max}$ is computed as

$$\sigma_{bias,max} = \max(|\overline{err} + 2\sigma_{err}|, |\overline{err} - 2\sigma_{err}|) \tag{15}$$

and stored as $B_{mount}^+ \approx |B_{mount}^-|$.

Finally, following the procedure described in [2], the total uncertainty $U_{95,bc}$ and its shift $\Delta U_{95,bc}$ are derived from

$$U_{95,bc} = \frac{1}{2} (\|\boldsymbol{B}^+\| + \|\boldsymbol{B}^-\|) \tag{16}$$

and from

$$\Delta U_{95,bc} = \frac{1}{2} (\|\boldsymbol{B}^+\| - \|\boldsymbol{B}^-\|) \tag{17}$$

respectively.

3.2. Results

Table I lists all elements in arrays $\boldsymbol{B}^+$ and $\boldsymbol{B}^-$.

Table I. Values for arrays $\boldsymbol{B}^+$ and $\boldsymbol{B}^-$.

Component$_i$	B_i^+ (°C)	B_i^+ (°C)
K-type thermocouple	1.500	-1.500
DAQ-6024E card	3.392	-3.368
SCXI-1102 module	1.158	-1.130
Thermocouple mounting error	0.087	-0.087

The total uncertainty thus calculated equals $U_{95,bc} = 3.87$ °C, while the shift reads $\Delta U_{95,bc} = 0.02$ °C; therefore, $U_{95,bc}^+ = U_{95,bc} - \Delta U_{95,bc} = 3.85$ °C and $U_{95,bc}^- = -U_{95,bc} - \Delta U_{95,bc} = -3.89$ °C.
As concerns random uncertainties, they are neglected. Nonetheless, in the next future $U_{95,bc}$ will be derived from end-to-end calibration data, as the method employed here seems to overestimate uncertainties. Consequently, random uncertainties will then be evaluated according to [2].

4. HEAT FLUX ASSESSMENT

4.1. Methodology

The main objective of this section is the assessment of the radial heat flux at the wet surface of the inner tube – namely, at $r_0 = 17.5$ mm. Thermocouples monitoring wall temperatures are again disregarded, as water channels are the only providing data close to r_0. If enough temperature data were available, the heat flux could be directly estimated from the temperature distribution in the radial direction

$$q''|_{r = r_0} = -k_{disc} \left.\frac{\partial T(r,\theta,z,t)}{\partial r}\right|_{r = r_0}, \tag{18}$$

where k_{disc} refers to the conductivity of the thermocouple discs [1]. However, since $T(r,\theta,z,t)$ is not inferable from the experimental data at our disposal, it is first conjectured that each thermocouple can be approximated as a one-dimensional body of length L (see Fig. 1), diffusivity α_{TC}, thermal conductivity k_{TC} and temperature distribution $T(x,t)$, with $x = 0$ at the thermocouple tip (that is, at r_0). The one-dimensional heat equation in Cartesian coordinates with constant α_{TC} can then be simplified as shown in Eq. (19), with initial and boundary conditions given by Eqs. (20), (21) and (22), $\widehat{T}_f(t)$ corresponding to $\widehat{\boldsymbol{T}}_f[1,j]$ from Subsection 3.1

$$
\begin{cases}
\dfrac{\partial T}{\partial t} = \alpha_{TC} \dfrac{\partial^2 T}{\partial x^2} & \text{(19)} \\[2mm]
T(x,0) = \hat{T}_f(0) & \text{(20)} \\[2mm]
T(0,t) = \hat{T}_f(t) & \text{(21)} \\[2mm]
\left(\dfrac{\partial T}{\partial x} \right)_{x=L} = 0 \,. & \text{(22)}
\end{cases}
$$

Eq. (21) assumes a large heat transfer coefficient between water and thermocouple tip. Conversely, Eq. (22) supposes that the heat transfer coefficient between thermocouple sheath and outer environment is small.

Now, as inferable from Fig. 5, the x-axis in Eq. (19) is either parallel or antiparallel to axis y_T, depending on the thermocouple location

$$
\frac{\partial T}{\partial y_T} =
\begin{cases}
\dfrac{\partial T}{\partial x} & \text{if } \hat{T}_f \in \widehat{\boldsymbol{T}}_{V1} \text{ or } \widehat{\boldsymbol{T}}_{V4} \\[3mm]
-\dfrac{\partial T}{\partial x} & \text{otherwise.}
\end{cases}
\tag{23}
$$
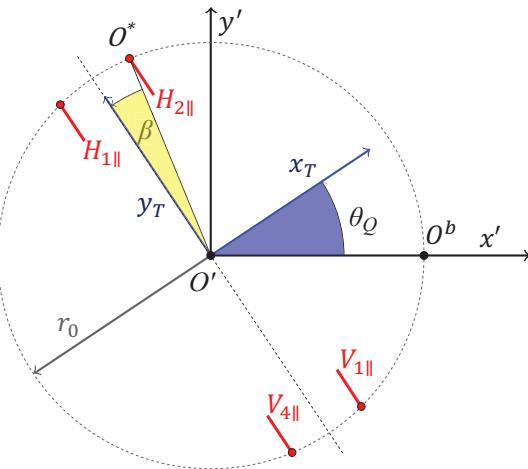
Fig. 5. Coordinate systems on a plane $z = $ constant, also called $x' - y'$ plane. The dashed circle represents the wet surface of the inner tube, while the dashed straight line depicts the centerline of the left and right thermocouple discs. All thermocouples, sketched as red segments, are parallel to this line, and hence not aligned with the radial heat flux. H3 and H4 are not shown as they are hidden under H1 and H2. Angle β, shown here larger than the real one, is enclosed by the centerline of the side thermocouple discs and by the line between the center O' and the red thermocouple tips.

Besides, each thermocouple is distinguished by a specific $\tilde{\theta}$, defined as the counterclockwise azimuthal angle between $\theta_Q = 0$ and the thermocouple tip lying on the circle with radius r_0. As in [1], θ_Q is the azimuthal angle read by the potentiometer.

Another quantity obtainable from experimental data is $\left(\dfrac{\partial T}{\partial \tilde{\theta}} \right)_{r=r_0}$, here approximated as

$$\left(\frac{\partial T}{\partial \tilde{\theta}}\right)_{r=r_0} \approx \begin{cases} \dfrac{\tilde{T}_{V1} - \tilde{T}_{V4}}{2\beta} \text{ if } \hat{T}_f \in \hat{\boldsymbol{T}}_{V1} \text{ or } \hat{\boldsymbol{T}}_{V4} \\[2mm] \dfrac{\tilde{T}_{H1} - \tilde{T}_{H2}}{2\beta} \text{ if } \hat{T}_f \in \hat{\boldsymbol{T}}_{H1} \text{ or } \hat{\boldsymbol{T}}_{H2} \\[2mm] \dfrac{\tilde{T}_{H3} - \tilde{T}_{H4}}{2\beta} \text{ otherwise.} \end{cases} \quad (24)$$

Now, thanks to the well-known formula for the rotation of a coordinate system, the following expression is deduced for the radial heat flux at the wall in terms of $\left(\frac{\partial T}{\partial \tilde{\theta}}\right)_{r=r_0}$ and $\left(\frac{\partial T}{\partial y_T}\right)_{r=r_0}$ only:

$$-\left(k\frac{\partial T}{\partial r}\right)_{r=r_0} = \frac{k_{disc}}{r_0 \tan(\tilde{\theta} - \theta_Q)}\left(\frac{\partial T}{\partial \tilde{\theta}}\right)_{r=r_0} - \frac{k_{TC}}{\sin(\tilde{\theta} - \theta_Q)}\left(\frac{\partial T}{\partial y_T}\right)_{r=r_0}. \quad (25)$$

The first term on the right-hand side of Eq. (25) is usually negligible, as can be surmised from Fig. 7. Consequently, in the next paragraphs, we will discuss whether our estimate of the second term on the right-hand side of Eq. (25) is correct, rather than try to assess the accuracy of the whole expression. As per Eq. (23), $\left(\frac{\partial T}{\partial y_T}\right)_{r=r_0}$ is found after solving Eq. (19); however, since Eq. (20) is merely an approximation, the heat flux calculated for $t \to 0^+$ should be taken cautiously.

Now, Eq. (19) can be solved either analytically or numerically. With respect to the numerical approach, Eq. (19) is discretized with the Crank-Nicolson finite difference scheme

$$T_q^{s+1}(1 + Co) - \frac{Co}{2}T_{q-1}^{s+1} - \frac{Co}{2}T_{q+1}^{s+1} = T_q^s(1 - Co) + \frac{Co}{2}T_{q-1}^s + \frac{Co}{2}T_{q+1}^s \quad (26)$$
$$\text{for } q = 1, \dots, N_x - 1, \quad s = 0, \dots, N_t - 1,$$

where the Courant number $Co = \alpha_{TC}\frac{\Delta t_1}{(\Delta x)^2}$ is selected so as to preserve the accuracy of the results. The time increment Δt_1 in the expression for Co is the inverse of the 100 Hz sampling rate [1]. The heat flux is then obtained by combining a fourth-order central difference approximation of the derivative in Eq. (23) with the other terms in Eq. (25).

Turning now to the analytical approach, Eq. (19) is assumed solvable thanks to Duhamel's theorem, which can be invoked only if $\tilde{\Theta}(x, 0) = 0$ [21], $\tilde{\Theta}(x, t)$ being a function of $T(x, t)$ satisfying Eqs. (19) and (22) as well. Thus, the simplest choice for $\tilde{\Theta}(x, t)$ is $\tilde{\Theta}(x, t) = T(x, t) - \hat{T}_f(0)$, so that Eqs. (19), (20), (21) and (22) are rewritten as

$$\begin{cases} \dfrac{\partial \tilde{\Theta}}{\partial t} = \alpha_{TC}\dfrac{\partial^2 \tilde{\Theta}}{\partial x^2} & (27) \\[3mm] \tilde{\Theta}(x, 0) = 0 & (28) \\[2mm] \tilde{\Theta}(0, t) = \Phi(t), \quad \Phi(t) = \hat{T}_f(t) - \hat{T}_f(0) & (29) \\[3mm] \left(\dfrac{\partial \tilde{\Theta}}{\partial x}\right)_{x=L} = 0. & (30) \end{cases}$$

Duhamel's theorem is then applied to an auxiliary problem where $\Phi(t) = 1$ and $\tilde{\Theta}(x, t)$ is called $\Theta(x, t)$ to differentiate it from the solution to Eq. (27). Thus, $\Theta(x, t)$ can be found as the superposition of a steady-state and a homogeneous solution [3]

$$\Theta(x, t) = 1 + \sum_{n=1}^{\infty} A_n \sin\left(\mu_n\frac{x}{L}\right)\exp\left(-\mu_n^2\frac{\alpha_{TC}t}{L^2}\right), \quad (31)$$

where μ_n and A_n are defined as $\mu_n = (2n-1)\frac{\pi}{2}$ and $A_n = -\frac{2}{\mu_n}$ respectively.

$\Theta(x,t)$ from Eq. (31) is then included in Duhamel's superposition integral [21]

$$T(x,t) - \hat{T}_f(0) = \Phi(0)\Theta(x,t) + \int_{\tau=0}^{t} \Theta(x,t-\tau)\frac{d\Phi}{d\tau}d\tau \tag{32}$$

so that the analytical solution to Eq. (19) is

$$T(x,t) = \hat{T}_f(t) + \sum_{n=1}^{\infty} A_n \sin\left(\mu_n \frac{x}{L}\right) \int_{\tau=0}^{t} \exp\left(-\mu_n^2 \frac{\alpha_{TC}(t-\tau)}{L^2}\right)\frac{d\Phi}{d\tau}d\tau \tag{33}$$

since here $\Phi(0) = 0$. As a result, the heat flux can be expressed as

$$-k_{TC}\left(\frac{\partial T}{\partial x}\right)_{x=0} = -k_{TC}\sum_{n=1}^{\infty} A_n \frac{\mu_n}{L} \int_{\tau=0}^{t} \exp\left(-\mu_n^2 \frac{\alpha_{TC}(t-\tau)}{L^2}\right)\frac{d\Phi}{d\tau}d\tau \tag{34}$$

from Fourier's law in Cartesian coordinates. It is relevant to note that this analytical solution is actually susceptible to discretization schemes, as the quantity $\frac{d\Phi}{d\tau}$ is usually approximated by finite-difference expressions. Thus, Eq. (34) can not be implemented as is: the heat flux will be underestimated if the infinite sum in Eq. (31) is truncated when additional terms become negligible, while convergence is lost or not achieved if the same simplification is applied to Eq. (34). Besides, integration by parts of the integral in Eq. (34) is not a viable option, as it would introduce local discontinuities for certain values of $\hat{T}_f(t)$.

A way to address these issues is to first rewrite the integral in Eq. (34)

$$I_n(t) = \alpha_{TC}\frac{\mu_n^2}{L^2}\int_{\tau=0}^{t} \exp\left(-\mu_n^2 \frac{\alpha_{TC}(t-\tau)}{L^2}\right)\frac{d\Phi}{d\tau}d\tau \tag{35}$$

as the Crank-Nicolson solution

$$I_n(v\,\Delta t_1) = \frac{\zeta}{1+\zeta}\left[\left(\frac{d\Phi}{dt}\right)_{\tau=v\,\Delta t_1} + \left(\frac{d\Phi}{dt}\right)_{\tau=(v-1)\,\Delta t_1}\right] + \frac{1-\zeta}{1+\zeta}I_n\big((v-1)\,\Delta t_1\big)$$
$$\text{for } v = 1, \dots, \frac{t}{\Delta t_1} \tag{36}$$

to the Cauchy problem

$$\begin{cases} \dfrac{dI_n}{dt} = \alpha_{TC}\dfrac{\mu_n^2}{L^2}\left(\dfrac{d\Phi}{dt} - I_n\right) & \tag{37} \\ I_n(0) = 0. & \tag{38} \end{cases}$$

In Eq. (36) $\zeta = \frac{\Delta t_1}{2L^2}\mu_n^2\alpha_{TC}$. Regarding thermal properties, both the analytical and the numerical approach resort to a harmonic mean of Chromel and Alumel properties

$$\chi = 2\frac{\chi_{Chromel}(\bar{T}_f)\chi_{Alumel}(\bar{T}_f)}{\chi_{Chromel}(\bar{T}_f) + \chi_{Alumel}(\bar{T}_f)} \text{ if } \chi = k_{TC} \text{ or } \alpha_{TC}, \tag{39}$$

where $\bar{T}_f$ is the arithmetic mean of $\widehat{T}_f$.

4.2. Verification and Results

The validity of the method described in Eq. (25) is currently under investigation. We lack experimental data to validate our heat-flux calculation, which was then verified with an analytical approach. Specifically, the wall heat flux from the temperature in Eq. (26) was compared with a formula given in the literature [4] which does not involve numerical integration or differentiation. This formula states that a linear heat flux with respect to time

$$q''_{th}(0,t) = q''_N \, Fo \tag{40}$$

is expected at the surface of a slab with the same initial and boundary conditions as in our case – namely, Eqs. (20), (21) and (22) –, if $\Phi(t)$ from Eq. (29) follows Eq. (41)

$$\Phi(t) = \frac{q''_N L}{k_{TC}} \left[\frac{Fo^2}{2} + \frac{Fo}{3} - \frac{1}{45} - \sum_{m=1}^{\infty} (-1)^{m+1} \frac{2}{m\pi^4} \cos(m\pi) \exp(-m^2\pi^2 Fo) \right], \tag{41}$$

where the Fourier number Fo is defined as $Fo = \alpha_{TC} \frac{t}{L^2}$ and q''_N is a normalizing heat flux.

If we denote the left-hand side of Eq. (34) by q''_{CN}, Fig. 6 (left) shows the time evolution of the quantity

$$err_0 = \left| \frac{\Delta q''_0(0,t)}{q''_{CN,max}(0,t)} \right|, \qquad \Delta q''_0 = q''_{CN} - q''_{th} \tag{42}$$

for $t > \Delta t_1$, since the accuracy of q''_{CN} is not deemed satisfactory for smaller times.
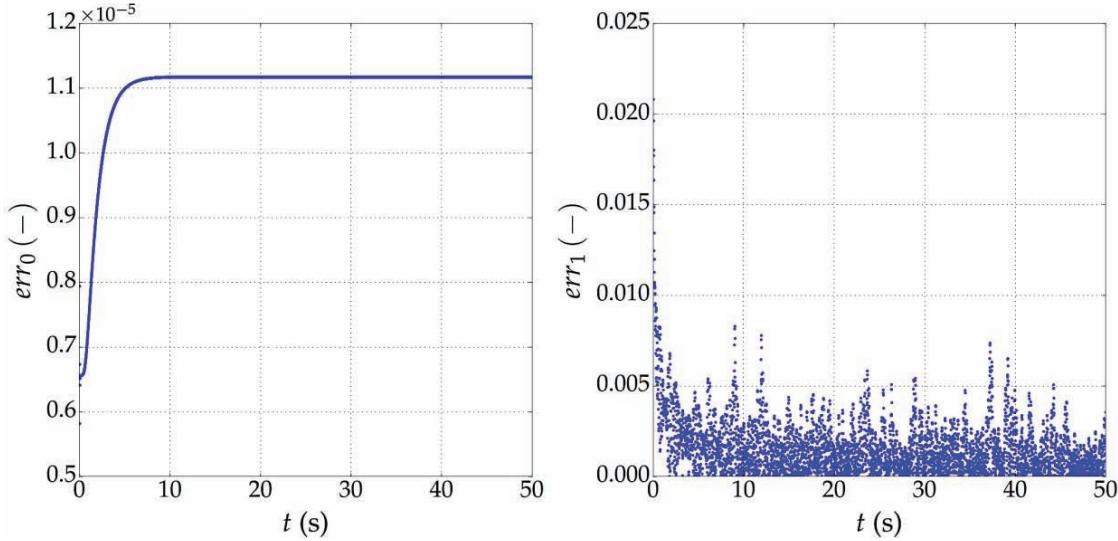
Fig. 6. Estimate of the normalized error for the CN scheme applied to the heat conduction equation. Both subplots were obtained with $Co = 1.268$. Left: a time-linear heat flux is expected at the thermocouple tip. Right: a sinusoidal water temperature is set at the thermocouple tip.

Now, if the fluid temperature at $x = 0$ $\widehat{T}_f(t)$ changes with time t according to Eq. (6) with $T_f \to \widehat{T}_f$, $f = 0.19$ Hz and $\Delta T = 10$ °C, an implementation of Eq. (34) as is would be unstable for $t \gg 0$ and prone to

truncation errors arising from the infinite sum of integrals. Hence, Eq. (36) was used to evaluate the integral term in Eq. (34). Fig. 6 illustrates the time evolution of the quantity

$$err_1 = \left| \frac{\Delta q_1''(0,t)}{q_{CN,max}''(0,t)} \right|, \qquad \Delta q_1'' = q_{CN}'' - q_{DI}'' \tag{43}$$

for $t > \Delta t_1$ since, as before, the accuracy of q_{CN}'' is not considered satisfactory for smaller times. Errors err_0 and err_1 in Fig. 6 are proved to be not significant, thus substantiating the validity of our procedure.

With respect to final results, Fig. 7 is obtained with $Co = 1.18$, which is deemed acceptable. As previously stressed, the first term on the right-hand side of Eq. (25) only contributes to a small percentage of the total radial heat flux, as depicted in Fig. 7 (right). The same behavior is observed regardless of label and (θ, z) position of water-side thermocouples, or of the boundary conditions in the experimental matrix. This implies that, even if the first term on the right-hand side of Eq. (25) were distorted by errors, the magnitude of the radial heat flux thus estimated would be virtually untouched.
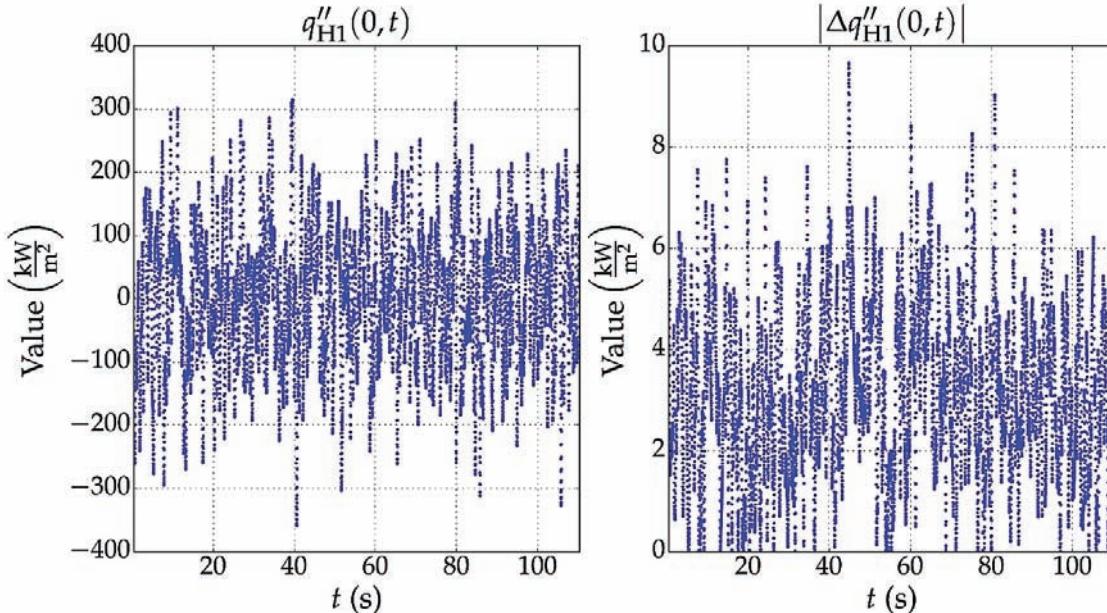
Fig. 7. Left: Radial heat flux close to thermocouple H1 (see Eq. (25)). Right: absolute value of the first term on the right-hand side of Eq. (25), here labelled as "azimuthal correction".

5. CONCLUSIONS

Six thermocouples inserted into special discs have acquired water temperatures in an annulus where non-isothermal turbulent streams flow and mix. The goal of these experiments is to study temperature fluctuations and thermal fatigue-induced stresses in those BWR control-rod stems around which an analogous mixing occurs.

Now, two topics have been extensively investigated here: the accuracy of the temperature readings, and methods for determining the heat flux at the annulus inner radius on the basis of the acquired data. As to accuracy, thermocouples have been first described with a two-dimensional finite-element model, which has then been verified by comparison with similar approaches from literature. Although this new model does not contribute to the evaluation of the highest uncertainty source, it is still of interest, since it can be further developed into a three-dimensional thermocouple model for future research on IHCPs.

Besides, a number of options for detrending time series and for mixing intensity parameters have been explored, which may lead to a better understanding of the mixing phenomenon and to additional studies on detrending and mixing intensity.

Regarding the radial heat flux, the data scarcity in the radial direction has compelled us to quantify it through a Crank-Nicolson discretization of the heat conduction equation applied to the thermocouples. This method has then been partially verified by comparison with an analytical solution and with a mixed analytical/computational one. Besides, it has been remarked that the order of magnitude of the azimuthal correction is overall small, which removes the need for a thorough verification of the corrected heat flux and strengthens the validity of our method. Nonetheless, a more complete, three-dimensional model of the thermocouple discs is currently under design, to include a wider range of variables in the assessment process.

NOMENCLATURE

Acronyms

CN Crank-Nicolson scheme

DI Duhamel's integral

Roman symbols

A number of unfiltered test-section samples per thermocouple channel from the first run at a certain (θ_Q, z_Q) pair [1] $\left(\frac{\text{samples}}{\text{iter ch}}\right)$

$\boldsymbol{B}$ bias array, or systematic uncertainty array (℃)

$\boldsymbol{B}^-$ negative-side systematic uncertainty array (℃)

$\boldsymbol{B}^+$ positive-side systematic uncertainty array (℃)

Bi Biot number

$\hat{C}_p$ specific heat at constant pressure $\left(\frac{\text{J}}{\text{kg K}}\right)$

h heat transfer coefficient $\left(\frac{\text{W}}{\text{m}^2\,\text{K}}\right)$

k thermal conductivity $\left(\frac{\text{W}}{\text{m K}}\right)$

N_t number of time intervals

N_x number of spatial nodes reduced by 1

(r, θ, z) cylindrical coordinate system fixed to the inner tube

$(\tilde{r}, \tilde{\theta}, \tilde{x})$ cylindrical coordinate system fixed to each thermocouple

S domain $\left(\text{m}^2\right)$

t time (s)

T temperature (℃, unless otherwise stated)

$\hat{\boldsymbol{T}}_f$ array of unfiltered, detrended test-section samples from a thermocouple channel (℃)

w finite element test function

w_1 weight

Greek symbols

α thermal diffusivity $\left(\frac{\text{m}^2}{\text{s}}\right)$

Γ boundary of the domain

Δx space increment (m)

Δt time step (s)

ρ density $\left(\frac{\text{kg}}{\text{m}^3}\right)$

σ standard deviation (℃)

Subscripts

b boundary

bc before calibration

f water

FE point R in Fig. 2

h finite-element mesh size

sw single-wire region

TC thermocouple

$H1$ thermocouple H1

$H2$ thermocouple H2

$H3$ thermocouple H3

$H4$ thermocouple H4

$V1$ thermocouple V1

$V4$ thermocouple V4

Superscripts

p finite-element time step

s finite-difference time step

REFERENCES

[1] H. Anglart, M. Bergagio, S. Hedberg and S. Rydström, "Measurement of Wall Temperature Fluctuations During Thermal Mixing of Non-isothermal Water Streams," in *Proceedings of the 16th International Topical Meeting on Nuclear Reactor Thermal Hydraulics, 30 Aug. – 4 Sept. 2015*, Chicago, 2015.

[2] J. Nakos, "Uncertainty Analysis of Thermocouple Measurements Used in Normal and Abnormal Thermal Environment Experiments at Sandia's Radiant Heat Facility and Lurance Canyon Burn Site," Sandia National Laboratories, 2004.

[3] F. P. D'Aleo and H.-M. Prasser, "Transient heat flux deduction for a slab of finite thickness using surface temperature measurements," *International Journal of Heat and Mass Transfer,* vol. **60**, pp. 616-623, 2013.

[4] J. Taler and P. Duda, Solving Direct and Inverse Heat Conduction Problems, Dordrecht: Springer, 2006.

[5] B. Shen, G. Xiao, C. Guo, S. Malkin and A. J. Shih, "Thermocouple Fixation Method for Grinding Temperature Measurement," *Journal of Manufacturing Science and Engineering,* vol. **130**, no. 5, p. 051014, 2008.

[6] R. Pyszko, M. Příhoda, P. Fojtík and M. Kováč, "Determination of Heat Flux Layout in the Mould for Continuous Casting of Steel," *Metalurgija,* vol. **51**, no. 2, pp. 149-152, 2012.

[7] Pentronic, "Tolerance Classes for Thermocouples According to the IEC 60 584-2:1995," [Online]. Available: http://www.pentronic.se/media/26434/IEC_60584_TC_060210.pdf. [Accessed 2 March 2015].

[8] Pentronic, "Thermocouple Metal-sheathed Probe with Miniature Connector - Model 8103000," [Online]. Available: http://www.pentronic.se/documenthandler.ashx?file=81LFDEXHRPQ1&filename=Pentronic%208103000%20En.pdf. [Accessed 2 March 2015].

[9] National Instruments, "SCXI-32 Channel Analog Input Modules," [Online]. Available: http://nees.org/data/get/facility/UMN/Equipment/821/SCXI_1102_Specs.pdf. [Accessed 2 March 2015].

[10] NIST, "Tables of Thermoelectric Voltages and Coefficients," [Online]. Available: http://srdata.nist.gov/its90/download/download.html. [Accessed 2 March 2015].

[11] National Instruments, "NI 6023E/6024E/6025E," [Online]. Available: http://www.ni.com/pdf/manuals/370719c.pdf. [Accessed 2 March 2015].

[12] R. B. Bird, W. E. Stewart and E. N. Lightfoot, Transport Phenomena, John Wiley & Sons, 2007.

[13] F. Hecht, "New Development in FreeFem++," *Journal of Numerical Mathematics,* pp. 251-265, 2012.

[14] K. Kato, M. Tagawa and K. Kaifuku, "Fluctuating Temperature Measurement by a Fine-wire Thermocouple Probe: Influences of Physical Properties and Insulation Coating on the Frequency Response," *Measurement Science and Technology,* vol. **18**, p. 779, 2007.

[15] M. Attia, A. Cameron and L. Kops., "Distortion in Thermal Field Around Inserted Thermocouples in Experimental Interfacial Studies, Part 4: End Effect," *Journal of Manufacturing Science and Engineering,* vol. **124**, pp. 135-145, 2002.

[16] C. Ould Lahoucine and A. Khellaf, "Dynamic Characterization of a Thermocouple in a Fluid Crossflow," *Sensors and Actuators A,* vol. **119**, pp. 48-56, 2005.

[17] K. Woodbury and A. Gupta, "Effect of Deterministic Thermocouple Errors (Bias) on the Solution of the Inverse Heat Conduction Problem," in *Proceedings of the 5th International Conference on Inverse Problems in Engineering: Theory and Practice*, Cambridge, UK, 2005.

[18] K. Dusarlapudi, B. Nashine, D. Bai and C. Babu, "Simulation of Fast Response Thermocouple for the Nuclear Reactor Core," in *Proceedings of the 2011 COMSOL Conference in Bangalore*.

[19] Material Property Database (MPDB) v. 7.79, North Reading, USA: JAHM Software Inc., 2014.

[20] C. Ould Lahoucine, "A Duhamel Integral Based Solution for the Sideways Heat Equation Applied to the Non-intrusive Temperature Measurement," *International Communications in Heat and Mass Transfer,* vol. **31**, no. 8, pp. 1037-1045, 2004.

[21] D. Hahn and M. Ozisik, Heat Conduction, John Wiley & Sons, 2012.